Title: Rare bioactive diffusible tau species from Alzheimer brain support both templated misfolding and fibril formation

Authors:
Noé Quittot[1,2]
Dhanush Sivasankaran[1,2]
Dorothea Böken[3,4]
Yu Chen[5,6]
Joshua E. Chun[1,2]
Anne E. Wiedmer[1,2]
Victoria Derosla[1,2]
Mariana B. M. S. Martins[1,2,7]
Forest A. Brooks[1,2]
Georg Meisl[3,4]
Matthew W. Cotton[3,4]
Durga G. Arumuganainar[8]
Theresa Connors[9]
Alexandra Melloni[9]
Mathew Frosch[9]
Derek H. Oakley[9]
Lee Makowski[5,10]
Meni Wanunu[5,6]
David Klenerman[3,4]
Bradley T. Hyman[1,2*]

Affiliations:
1. Department of Neurology, Massachusetts General Hospital, Boston, MA, USA
2. Harvard Medical School, Cambridge, MA, USA
3. UK Dementia Research Institute at the University of Cambridge, Cambridge, UK
4. Yusuf Hamied Department of Chemistry, University of Cambridge, Cambridge, UK
5. Department of Bioengineering, Northeastern University, Boston, MA, USA
6. Department of Physics, Northeastern University, Boston, MA, USA
7. Technical University of Munich, Munich, Germany
8. Bioinformatics Program, Northeastern University, Boston, MA, USA
9. Department of Pathology, Massachusetts General Hospital, Boston, MA, USA
10. Department of Chemistry and Chemical Biology Northeastern University, Boston, MA, USA

***Corresponding author:** Bradley T Hyman bhyman@mgh.harvard.edu

Abstract

In Alzheimer's disease, both classical neurofibrillary tangles, and diffusible, aqueous soluble (High Molecular Weight, or HMW) species are able to support templated misfolding. How these tau proteoforms relate is uncertain. Using sequential size exclusion and anion exchange chromatography, we fractionated the HMW tau population and found both seed competent, and seed not competent proteoforms. Super resolution, atomic force, and immunogold electron microscopy confirmed that the size and conformation of both bioactive and non-bioactive tau proteoforms are similar, with dimers, trimers, and tetramers predominating. The presence of surface phosphorylation correlates with seeding capacity. Bioactive tau at fMol concentrations can induce seeding in a reporter cell. The soluble bioactive species support aggregation of a truncated repeat domain tau construct into thioflavin T positive fibrils and retain seeding activity over serial amplification in vitro and in cellulo, whereas non-bioactive oligomeric species do not. Together, these findings indicate that oligomeric assembly is required but not sufficient for seeding; instead, specific biochemical attributes of a rare oligomeric tau subset confer self-propagating, prion-like templated misfolding.

Keywords: Alzheimer's disease, human brain tissue, Tau, oligomer, seed, bioactive species, non-bioactive species, phosphorylations, prion-like mechanism, super resolution microscopy, RT-QuIC.

Introduction

In Alzheimer's disease (AD), cognitive decline correlates with the hierarchal propagation of tau from medial temporal lobe areas to limbic and association areas[1,2], consistent with a templated misfolding mechanism of tau seeding and disease progression[3]. Potentially pathological tau is present in a wide variety of tau conformations including classical fibrillar neurofibrillary tangles (NFTs) as well as more recently described diffusible, aqueous soluble, highlighting the structural diversity of the protein[4]. While NFTs were historically considered to be associated with neuronal loss and toxicity, many studies have now shown that intermediate species can also be harmful to the brain[5,6]. In animal models it has been shown that oligomer formation precedes the appearance of NFTs and the spreading is associated with cognitive deficits and neurodegeneration[7-10]. In human AD brains, conformationally specific antibodies detect tau pathology prior to and distinct from classical tangles[11]. Tau oligomer levels are elevated in the absence of NFTs, tau competent seeds are found in synaptically connected networks preceding the formation of NFTs[12,13], and the amount of tau bioactivity present in the diffusible, aqueous soluble fraction of the brain corresponds with clinical rate of progression in AD[14,15]. While the presence of oligomers is supported by a growing body of evidence, their molecular identity is largely uncertain, and it is unknown how their size and biochemical signature relate to their bioactivity. To date, there is no consensus on how to define tau seeds, particularly in terms of biophysical and biochemical attributes, and whether they are potent amplifiers of structural information.

In an attempt to characterize and identify tau seeds among the numerous varieties of tau species, we reported that high molecular weight (HMW) tau isolated via size exclusion chromatography (SEC) from human brain can be taken up by neurons and induce tau aggregation[16]. This represented <1% of all soluble tau present in the AD cortex. However, this semi-purified fraction, based only on size, is not homogeneous. For example, tau immunoprecipitation methods with monoclonal antibodies directed against various PTMs are not equivalent in removing bioactivity of the HMW samples, suggesting the presence of multiple species[14]. Therefore, in this study we have used a combination of biochemical approaches to fractionate the HMW tau population and revealed the presence of numerous subspecies including both seed competent and non-seed competent species. Moreover, we show that the seed competent species, or bioactive seeds, are retained on an anion exchange column, are sensitive to phosphatase treatment, are oligomeric as imaged with immunoelectron microscopy, super resolution microscopy, and atomic force microscopy, and has phospho-epitopes displayed on the surface. These further purified species can replicate *in vitro,* and daughter seeds generated from the bioactive species induce tau aggregation both *in vitro* and *in cellulo*, whereas daughter seeds derived from non-bioactive oligomeric species remain inactive. These data suggest that seed

competence is not dictated by oligomeric state alone and require specific biochemical properties that enable propagation of aggregation over serial passages, consistent with prion-like templated misfolding.

The heterogeneity of aqueous, diffusible tau species—and the absence of consensus biophysical criteria for what constitutes a "seed"—has led to substantial variability in nomenclature across the literature. Here, we use the term "high molecular weight" tau to refer to the characteristic of tau isolated from disease brains as eluting from a size exclusion column in a "high molecular weight" (e.g. several hundred kD) fraction. By contrast, low molecular weight refers to the monomeric tau that elutes from a size exclusion column at the expected molecular weight of tau, and is also referred to as "physiological tau". We use oligomeric tau to describe small assemblies of tau molecules, not necessarily implying a specific number or specific structure. Fibrils are generally defined as having a β pleated sheet structure, and are observed in Alzheimer tissue as neurofibrillary tangles. Short fibril species are either building blocks or small fragments of the large fibrillar structures that can be observed neuropathologically. The nature of the smallest fragments makes definitive structural determination difficult, in that molecular definition is not possible short of cryoEM, but structures that are not repeated, are not purified, or are not unique are difficult to resolve by cryo-EM. Other biophysical methods, such as those used here including transmission immunoelectron microscopy, atomic force microscopy, and super resolution microscopy do not have sufficient resolution to observe molecular structure directly, but do provide insight into the nature of tau containing assemblies. Because of these limitations, we refer to the material studied here as aqueous diffusible assemblies, and use the term "high molecular weight" to reflect their characteristics on size exclusion columns. While fibrils were not observed in any of our experimental preparations, the possibility that there are some short fibrils cannot be definitively ruled out.

Methods

Human tissue and data collection

Nine human participants with AD were selected from the Massachusetts Alzheimer's Disease Research Center Longitudinal Cohort study on the basis of the following criteria: (1) clinically diagnosed with dementia due to probable AD; (2) cognitive status assessed at least three times by a neurologist at the Massachusetts General Hospital (MGH) Memory Clinic Unit and scored using CDR-SOB; (3) diagnosis of AD confirmed postmortem by an MGH neuropathologist; (4) Braak Neurofibrillary tangles (NFTs) stage V or VI as determined by the location of NFTs with a total tau immunostaining[17]; and (5) concurrent pathologies considered to be clinically non-significant. Age of onset, age at death, postmortem interval and sex were also collected and are listed in Supplementary Table 1. Autopsy tissue from human brains were collected at MGH, with informed consent and approval of local institutional review boards. Human brains were processed as previously described[13]. Briefly, all brains were separated into 2 hemispheres, one of which

118 was initially sliced coronally at the time of autopsy and 1-cm-thick slabs were immediately flash frozen and
119 stored at −80 °C. Approximately 5 g of frontal cortex was dissected out of the frozen brain section
120 corresponding to Brodmann Area 8 and kept at −80 °C until homogenization.

121 **Tissue brain homogenization**

122 Frozen human tissue (5g) was thawed on wet ice, and gray matter was dissected and then immediately
123 homogenized in PBS containing 1X protease and phosphatase inhibitors (Cell Signaling, #5872) + 2 µM
124 Trichostatin A (Sigma, #T8552) in a 15-ml glass Dounce homogenizer. The tissue was Dounce
125 homogenized with 30 up and down strokes on ice by hand. The homogenate was centrifuged at 10,000g for
126 10 min at 4 °C. The supernatant was collected and aliquoted to avoid excessive freeze–thaw cycles.

127 **Tau seed enrichment**

128 Each chromatographic step was performed on a fast protein liquid chromatography (FPLC) apparatus
129 (ÄKTA Pure 25L, GE Healthcare) at 4°C. All buffers were filtered through a 0.2-µm membrane filter and
130 cooled down to 4°C before use.

131 **Size exclusion chromatography (SEC)**

132 5 mL of brain PBS extracts were separated by SEC on a single HiLoad 16/600 Superdex 200 pg column
133 (no. 28989335, Cytiva) in Tris 20 mM, pH 8.6 at a flow rate of 1 $ml.min^{-1}$. Fractions of 2 mL were retrieved
134 and analyzed by western blots, and subjected to the *in vitro* seeding assay. Fractions containing bioactive
135 HMW tau species were pooled.

136 **Anion exchange chromatography (AIEX)**

137 5mL of HMW tau species were enriched via a high-resolution and strong anion exchange chromatography
138 medium, consisting of non-porous 3 µm monodisperse beads, using a Mini Q 4.6/50 PE column (no.
139 17517701, Cytiva). HMW tau species were captured on the resin with a starting buffer of Tris 20 mM,
140 pH 8.6 and eluted by applying a 20 mL linear gradient, or step-wise elution, with Tris 20 mM + 4 M NaCl,
141 pH 8.6 at a flow rate of 0.25 $ml.min^{-1}$. Fractions of 0.5 mL were retrieved and analyzed by dot blot and the
142 *in vitro* seeding assay. Fractions containing non-bioactive and bioactive HMW tau species were pooled
143 separately.

144 **Desalting column**

145 Following AIEX, non-bioactive and bioactive HMW tau species were buffer exchanged on a HiTrap
146 desalting column (no. 29048684, Cytiva) to phosphate-buffer saline (PBS) at flow rate of 5 $ml.min^{-1}$. A
147 minimum threshold of 5 mAU was set to start/stop collection. Conductivity was monitored to evaluate the
148 buffer exchange from a low salt to a high salt buffer.

149 **Western Blots and Silver Stain**

150 NuPAGE LDS Sample Buffer (ThermoFisher, NP0007) and NuPAGE Sample Reducing Agent
151 (ThermoFisher, NP0009) were added to tau seeds, boiled for 5 min at 95 °C and run on 4–12% Bis-Tris
152 SDS–PAGE (Invitrogen) in MOPS buffer (Invitrogen). The gels were stained with silver stain following
153 manufacturer instructions (Pierce™ Silver Stain Kit, no. 24612) or transferred to a nitrocellulose membrane
154 (NP0324BOX) using an Invitrogen™ iBlot™ 2 Gel Transfer Device (IB21001). Blots were incubated with
155 blocking buffer (Intercept TBS blocking buffer, Li-Cor, no. 927-60001) for 30 minutes followed by
156 incubation with a monoclonal rabbit anti-pan-tau 1:1,000 (D5D8N, no. 43894, from Cell Signaling)
157 overnight at 4 °C or 1h at room temperature. Blots were washed three times for 10 min with TBS-T and
158 incubated with secondary anti-rabbit IRDye680 or IRDye800 (1:10,000) for 1 h at room temperature and
159 imaged on the Odyssey infrared imaging system (Li-Cor).

160 **Dot Blots**

161 30 to 100 µL of fractions were loaded on a nitrocellulose membrane using a 96-well dot blot apparatus (Bio-
162 Rad, no. 1706545) and incubated for 30 min at room temperature before proceeding to vacuum filtration.
163 Blots were then processed as described in the western blot section. Dot blot intensities were quantified by
164 by densitometric analysis in Image J (Fiji).

165 **Two-dimensional gel electrophoresis (2D gel)**

166 30 µL of the sample was mixed with 1.4 µL Blue Bromophenol 1% and 108.6 µL rehydration buffer
167 (BioRad #1632106). The mix was loaded in a 7 cm running chamber of a six-enclosed channels cassette
168 (ThermoFisher, ZM0003). A 7-cm IPG strip with a non-linear gradient pH ranging from 3 to 10
169 (ThermoFisher, ZM0018) was added to the running chamber containing the sample mix. The cassette was
170 sealed and incubated for 1 hour at room temperature. For the first dimension, the cassette was placed in the
171 IPG runner mini cell (ThermoFisher, ZM0001), and the outer chamber was filled with 600 mL of deionized
172 water. The isoelectric focusing was performed using ZOOM™ Dual Power Supply (100-120 VAC 47 - 60
173 Hz) (ZP10001) with the following sequence: 1) 175 V for 30 min; 2) 175 to 2000 V over 90 min; 3) 2000 V
174 for 60 min. For the second dimension, strips were incubated with NuPAGE LDS Sample Buffer
175 (ThermoFisher, NP0007) and NuPAGE Sample Reducing Agent (ThermoFisher, NP0009) using an
176 equilibration tray (ThermoFisher, ZM0007) at room temperature for 15 min. Strips were then loaded on
177 NuPAGE™ Bis-Tris Mini Protein Gels, 4–12%, 1.0–1.5 mm (NP0330BOX) and sealed by adding 0.5%
178 agarose mixed with MOPS running buffer. Electrophoresis is performed in two steps: 1) 100 V for 15 min
179 followed by 2) 175 V for 60 min. Gels were then uncast and transferred to a nitrocellulose membrane as
180 previously described.

181 **Dephosphorylation**

182 HMW tau was subjected to dephosphorylation using Lambda Protein Phosphatase (LPP) kit (New England
183 Biolabs (NEB), #P0753S). Two reaction mixes were prepared: one containing LPP at concentration of 800
184 units/mL and another without the enzyme. Each reaction was performed with NEB buffer for Protein
185 MetalloPhosphatases, 1 mM $MnCl_2$, 1X Protease Inhibitor Cocktail. Both reaction mixes were incubated at
186 30 °C for 2 hours. To inactivate phosphatase, samples were heated at 65 °C for 1 hour. Samples were then
187 centrifuged at 15 000g for 10 minutes at 4 °C to pellet precipitated enzymes. The supernatants were collected
188 and stored at –20 °C for further analysis.

189 **Atomic Force Microscopy**

190 To characterize the morphology of the bioactive and non-bioactive tau species, 5µL protein samples were
191 mixed with 5µL phosphate-buffered saline (PBS). This mixture was subsequently deposited onto a freshly
192 cleaved mica substrate and allowed to incubate for 10 minutes. Following incubation, the mica surface was
193 rinsed with deionized water (DI) to remove unbound proteins and then dried under a gentle stream of
194 nitrogen. The dried protein samples were imaged were imaged utilizing a MultiMode 8 AFM and Nanoscope
195 V controller (Bruker, Billerica, MA, USA) performed in ScanAsyst in air mode using a ScanAsyst-air
196 silicon tip (Bruker). The collected imaging data were processed using NanoScope Analysis software
197 (Bruker) and further analyzed by Gwyddion software.

198 **Single-molecule pull-down (SiMPull)**

199 Single-molecule pull-down (SiMPull) super-resolution microscopy was performed as previously
200 described[18] with slight modifications. Briefly, passivated PEGylated glass coverslips were incubated with
201 biotinylated capture antibody (10 nM in blocking solution: 1mg/mL BSA in PBS) for 10 minutes. This was
202 followed by washing twice with PBST (0.05% Tween-20 in PBS) and once with 1% Tween-20 in PBS and
203 then 10 minutes incubation in blocking solution. After a PBST wash, 10µL of biological samples (1:2
204 dilution in PBS) was added and left to incubate for 1 hour at room temperature, followed by washing in
205 PBST twice and 1% Tween-20 and 30 minutes incubation in blocking solution. Detection antibody
206 covalently labelled with a docking strand (DBCO TEG-
207 AAACCACCACCACCACCACCACCACCACCACCACCACCA) for DNA PAINT was incubated (3nM in 0.1
208 mg/mL BSA in PBS) for 15 minutes, followed by washing in PBST twice, 1% Tween-20 and PBS. Last,
209 3µL imaging strands (1 nM in PBS, TGGTGGT-atto655) were added before the gasket was sealed with a
210 clean coverslip.

211 **Super resolution image acquisition and analysis**

212 Imaging was performed on a home-built total internal reflection fluorescence (TIRF) microscope,
213 comprising an inverted Ti-2 Eclipse microscope body (Nikon) with a 1.49 N.A., 60x TIRF objective (Apo
214 TIRF, Nikon) and a perfect focus system. Images were acquired for 8000 frames of 100 ms exposure using

215 a 638 nm laser (Cobolt 06-MLD-638, HÜBNER) and were collected in a grid using an automated script
216 (Micro-Manager) to avoid any bias in the selection of the field of views. Super-resolution images were
217 reconstructed and analyzed as described in Böken *et al.*, 2024[18]. Briefly, localizations were identified and
218 fit using ComDet then corrected for microscope drift using the inbuilt implementation of redundant cross-
219 correlation. Localizations were filtered for precision <30 nm before DBSCAN clustering was performed
220 using the scitkit-learn package with permissive parameters (radius of 0.3 and minimum density of 5). The
221 skeletonized length of each aggregate was measured whereby the length of each aggregate is reported as the
222 summed branch distance. Finally, super-resolved images were rendered using the inbuilt Picasso
223 functionality.

224 **Single Molecule Array (SIMOA)**

225 Simoa assays were developed using the Quanterix HomeBrew set up. Bead conjugation was performed as
226 per the manufacturer's instructions using Quanterix reagents. Briefly, 488 dye-coated paramagnetic
227 carboxylated beads were activated with EDC at 4°C, washed, and subsequently conjugated to antibody,
228 followed by blocking of the beads. The antibody coating efficiency was determined by measuring the
229 residual antibody concentration in the solution and supernatant of the first wash. Beads were pelleted and
230 stored in Bead Diluent Buffer at 4 °C. Simoa plates were prepared in a "3-step-assay" following the
231 Quanterix protocol. Samples were diluted in tau 2.0 sample diluent, and added to a Simoa 96-well plate
232 (100 µL). Approximately 500k antibody-conjugated beads were added to each well and incubated (30°C,
233 800 rpm, 30 min). All washing steps were performed using the automated 3-step-assay program on the
234 Simoa Microplate Washer. After three automated washes with Simoa wash buffer A, each well was
235 incubated with 100 µL biotinylated detection antibody (0.3 µg/mL in Detector/Sample diluent, 30°C, 800
236 rpm, 10 min), followed by three further washes with Simoa wash buffer A. SBG (streptavidin β-
237 galactosidase) enzyme was added to each well (150 pM in SBG Dilution buffer and incubated (30°C, 800
238 rpm, 10 min), followed by three washes with Simoa wash buffer A and two washes with Simoa Wash Buffer
239 B. The beads were left to dry for 10 min and processed on the Quanterix SR-X™ Instrument using RGP as
240 substrate. The readout is determined as the fraction of beads with enzyme activity (f_{ON}), which calculates
241 the average enzymes per bead (AEB) assuming Poisson statistics. For aggregate-specific assays, any sample
242 or calibrant concentrations with $f_{ON} > 0.7$ was avoided. Lysate from cells overexpressing tau aggregates was
243 used as a calibration standard[19]. After obtaining the AEB values at each calibration level, a four-parameter
244 logistic (4PL) curve was fitted.

245 **Negative-stain electron microscopy**

246 For negative stain electron microscopy, 3 µL of the desired sample was applied to a 200 mesh Cu
247 Formvar/Carbon grid and incubated for two minutes before the excess liquid was wicked dry and the grid

248 was washed with 3 µL of water. The grid was then wicked dry again and 3 µL of 2% uranyl acetate was
249 applied for 90 seconds before being wicked and allowed to dry. Images were recorded using a JEOL 1011
250 transmission electron microscope.

251 **Immunogold labeling for electron microscopy and image analysis**

252 Sample application followed the same steps as outlined for negative-stain electron microscopy. Then, the
253 grid was placed sample side-down onto a drop (15-20 µL) of blocking buffer (PBS + 0.1% gelatin) on a
254 piece of parafilm. Parafilm is placed on a platform in a water dish to maintain humidity. The grid was then
255 left in blocking buffer for 10 minutes. Then, the grid was placed onto a drop of diluted primary antibody (in
256 blocking buffer) for 3 hours. The grid was then washed by being transferred to a drop of blocking buffer for
257 3 minutes. This was repeated for a total of 4 washes. The grid was then transferred to a drop of undiluted
258 gold conjugated secondary antibody for 1 hour. The grid was subsequently washed by being transferred to
259 a drop of PBS for 3 minutes. This was repeated for a total of 2 PBS washes, and 2 water washes. If double-
260 labeling, grid was placed into a new primary antibody and underwent the following steps (a different size
261 gold particle-conjugated secondary antibody was used). Once the final water wash was wicked away, 3 µL
262 of 2% uranyl acetate was applied for 90 seconds, then wicked dry. Images were recorded using a JEOL
263 1011 transmission electron microscope. Histograms of distances between gold particles were generated by
264 determining the (x,y) coordinates of the center of each gold particle in an electron micrograph using the
265 'Analyze Particles' utility in ImageJ. Additional processing utilized a simple Python script that (i) calculated
266 the distance between each gold particle pair; (ii) Calculated a raw histogram by binning the inter-particle
267 distances; (iii) divided the number of particles in each bin by the mean gold-gold distance of the
268 corresponding bin. This produced a plot of number density (relative frequency) of particles at each distance.
269 This number density was then normalized to facilitate comparison of results from different samples. The
270 resulting 'histograms' thereby provide a measure of how the presence of a gold particle influences the
271 number density of gold particles in its vicinity.

272 **RT-QuIC assay**

273 Real-time Quaking-Induced Conversion (RT-QuIC) assays were performed by incubating biological
274 samples with two different tau substrates. 1) A Tau fragment corresponding to the AD core, residues 306–
275 378, was used at a final concentration of 10 µM in an assembly buffer composed of 100 mM NaCl, 10 mM
276 HEPES, and 1 mM TCEP, as described in Carlomagno *et al.*, 2021[20]. 2) Recombinant tau isoforms 0N4R
277 and 0N3R were combined at a 2:3 ratio to a total protein concentration of 10 µM in PBS. Biological samples
278 were added at 2 µL per well and incubated with each substrate mixture. Thioflavin T (ThT) was included in
279 each reaction to a final concentration of 25 µM. Reactions were carried out in 40 µL total volume, in
280 triplicate, in sterile, sealed 384-well black-walled, clear-bottom, nonbinding microplates (Corning). Kinetic

281 assays were conducted at 37 °C using a FLUOstar Omega plate reader with continuous orbital shaking at
282 200 rpm. ThT fluorescence (excitation: 440 nm; emission: 485 nm) was measured every 15 minutes from
283 the bottom of the plate to monitor fibrillization. In separate wells, conditions were replicated without ThT
284 used for negative stain electron microscopy and second run of seeds amplification.
285 Kinetic data from triplicates were averaged and the lag time (t_{lag}), defined as the time before any detectable
286 amyloid forms, was determined with a Boltzmann sigmoidal curve,

287 $$F = \frac{F_0 + (F_{max} - F_0)}{1 + e^{-(t-t_{50})/k}}$$

288 where t_{50} is the time to half-maximum intensity, k is the apparent first-order rate constant, and F_0 and F_{max}
289 are the minimum and maximum fluorescence intensities, respectively. The lag time was then calculated
290 using the formula $t_{lag} = t_{50} - 2k$.

291 **Seeding assay:**

292 **<u>In vitro tau seeding FRET-biosensor assay.</u>** The *in vitro* seeding assay has been previously described and
293 widely characterized[21]. Briefly, the Tau RD P301S FRET Biosensor (ATCC CRL-3275) cells stably
294 expressing the repeat domain of tau with the p.P301S mutation conjugated to either cyan fluorescent protein
295 (CFP) or yellow fluorescent protein (YFP) (TauRD-P301S-CFP/YFP) were cultured at 37 °C, 5% CO2 in
296 DMEM, 10% vol/vol FBS, 0.5% vol/vol penicillin–streptomycin. Cells were plated on Costar Black, clear-
297 bottom 96-well plates (previously coated with 1:20 poly-D-lysine) at a density of 20,000 cells per well. The
298 same volume of brain extracts (2.67 µl per well) was then incubated with Lipofectamine 2000 (Invitrogen,
299 final concentration 1% vol/vol) in opti-MEM (final volume of 50 µl per well) for 10 min at room temperature
300 before being added to the cells. Each condition was applied in triplicate. Tau seeding was subsequently
301 analyzed using flow cytometry.

302 **<u>Flow-cytometry seeding analysis.</u>** After 24 h, medium was removed, and 50 µl trypsin 1× was added for 7
303 min at 37 °C. Chilled DMEM + 10% FBS (150 µl) was added to the trypsin, and cells were transferred to
304 96-well U-bottom plates (Corning). Cells were pelleted at 500g, resuspended in freshly made 2% vol/vol
305 paraformaldehyde in PBS (Electron Microscopy Services) for 10 min at room temperature in the dark, and
306 pelleted at 500g. Cells were resuspended in chilled PBS and run on the MACSQuant VYB (Miltenyi) flow
307 cytometer. CFP and FRET were both measured by exciting the cells using the 405-nm laser and reading
308 fluorescence emission at the 405/50-nm and 525/50-nm filters, respectively. To quantify the FRET signal,
309 a bivariate plot of FRET versus the CFP donor was generated, and cells that received control brain extract
310 alone were used to identify the FRET-negative population. Using this gate, the tau seeding value for each
311 well was calculated by multiplying the percentage of FRET-positive cells by the median fluorescence

312 intensity of that FRET-positive population. We analyzed 40,000 events per well. Data were analyzed using
313 the MACSQuantify software (Miltenyi).
314 **Fitting of single hit dynamics.** Fitting a one hit model to the seeding titration data shows good agreement.
315 The one hit model applies to systems where a single seeding event is required to trigger the production of
316 daughter seeds. A system with a low seeding efficiency can still show one hit dynamics, however a much
317 larger concentration of seed will be needed to see the same response if the seeding efficiency is lower.
318 Whether a system shows one hit dynamics or not will depend on the seeds and the cells/system that is being
319 treated. We fit the following functional form to the data that calculates the number of positive cells given a
320 specific concentration of seeds,
321
322 $$Number\ Positive\ Cells = N\left(1 - e^{-\lambda C}\right) + B,$$
323
324 where N is the total number of cells, λ is the seeding efficiency and C is the seed concentration. The final
325 term, B, is an additional baseline of cells that would test positive independent of seed. We set $B = 3$ based
326 on the positive baseline observed in control experiments. For the bioactive species, the best fit for the data
327 set is given when $N = 950$ and the seeding efficiency $\lambda = 1.3 \times 10^{-4}$ fM^{-1}. We use the same baseline and
328 total number of cells to estimate the seeding efficiency in the non-bioactive data. There is no pronounced
329 dose response in the non-bioactive data; most seed concentrations give essentially the same number of
330 positive cells. We therefore only consider the highest three seeding concentrations where a dose-response
331 may be emerging. This gives the non-bioactive seeding efficiency as $\lambda = 5.3 \times 10^{-6}$ fM^{-1}. As even at those
332 highest three points, the response to seeding is weak compared to background, this should be interpreted as
333 an upper bound on the seeding efficiency of the non-bioactive species.
334 **Antibodies**
335 D5D8N and HT7 are both monoclonal antibodies directed against a central tau epitope (~residue 160) and
336 detect all six canonical CNS tau isoforms and hence are referred as pan-tau antibody; however, it may not
337 detect truncated fragments lacking this region.
338 AT8 is a monoclonal antibody directed against phosphoresidues Ser 202 and Thr 205.
339 pT181, pT217, pT231, pS262, pS356, pS396, pS404 are monoclonal antibodies directed against indicated
340 residues (S: Serine, T: Threonine) at the indicated position.
341 PHF1 is a monoclonal antibody directed against phosphoresidues pS396 and pS404.

342 **Results**

343 **High-molecular-weight tau contains various subspecies, with the phosphorylated forms being the**
344 **most seeding-competent.**

Initial analysis by two-dimensional gel electrophoresis revealed that HMW tau isolated from nine human AD brains consisted of a heterogeneous population of molecules with isoelectric point (pI) values ranging from 5 to 8.5, indicating a mix of modified and unmodified tau species (Supplementary Figure 1). Given that phosphorylation is the predominant modification, we hypothesized that its removal would significantly impact the net charge and seeding activity of HMW tau. To test this, we treated HMW tau with lambda protein phosphatase (Lambda PP) to assess whether we could reduce the seeding activity (Figure 1A). Dephosphorylation significantly reduced tau's bioactivity, as measured by the FRET reporter HEK cell assay[21] (Figure 1B). This finding aligns with prior studies showing that dephosphorylation diminishes tau's seeding competency[16,22], and with our previous observation of a positive correlation between the extent of post-translational modifications (PTMs) and the bioactivity of HMW tau[23]. Dot blot analysis confirmed the loss of immunoreactivity for the tau phospho-specific AT8 antibody, while tau levels assessed with pan-Tau antibody remained unchanged (Figure 1D, E). In summary, these results indicate that the HMW tau population includes a mix of modified molecules, with highly charged, phosphorylated species being the most bioactive.

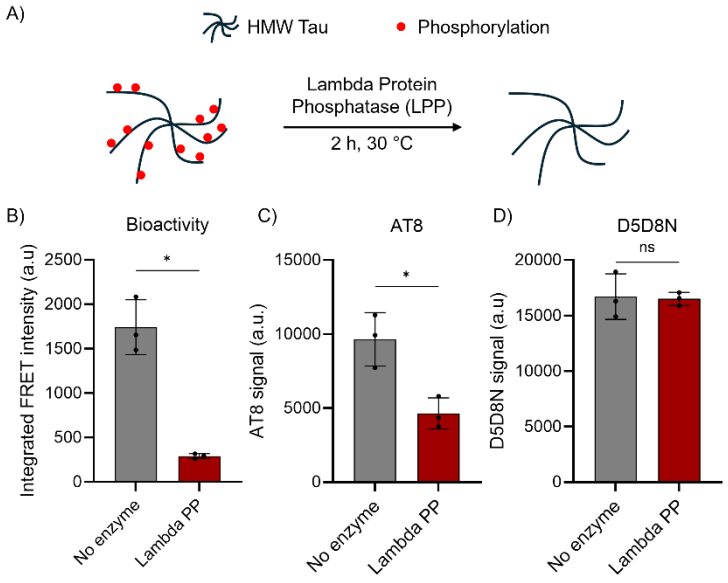

Figure 1. Dephosphorylation of human-derived HMW tau species decreases bioactivity.
*A) Schematic representation of HMW tau dephosphorylation by the Lambda Protein Phosphatase (LPP). B) Seeding activity assay using FRET reporter HEK cell; the integrated FRET intensity was quantified by flow cytometry. Data represents mean ± S.D. of three individual experiments performed in triplicate with HMW Tau isolated from the AD case 1971. Results were analyzed using the paired student t-test, * for*

367 *$p < 0.05$ and ns for non-significant. C), D) Dot blot quantification of HMW tau, originating from the same*
368 *case as panel B, treated or not with Lambda PP and probed with the anti-phospho tau AT8 or the pan-tau*
369 *antibody D5D8N.*

370 **Both non-bioactive and bioactive species are found in the HMW tau population.**

371 Given the variation in apparent pI of tau species from the early SEC fractions observed by 2D gel, we further
372 separated the HMW fraction using a technique sensitive to variations in surface charge. Considering that
373 phosphorylation adds two negative charges at physiological pH, while acetylation or ubiquitination
374 neutralizes lysine side chains, we hypothesized that more negatively charged modified and most bioactive
375 tau species will interact more strongly with the resin and be eluted in later fractions. This strategy has proven
376 to be efficient in separating unmodified and phosphorylated tau produced in yeast and SF9 insect cells [24,25].
377 Therefore, following SEC, the collected HMW Tau was applied to an anion exchange column. Elution
378 profiles for Tau and phosphorylated Tau were then determined under native conditions using dot blot
379 analysis, with the pan-Tau antibody D5D8N and the phospho-specific antibody AT8, respectively. The
380 corresponding seeding activity of each eluted fraction was determined with the previously mentioned cell-
381 based assay. Interestingly, we observed that tau was eluted in nearly all the fractions along the linear elution
382 gradient, confirming the presence of multiple tau species varying in their binding capacity to the resin,
383 suggesting species with varying overall net charge and/or conformations (Figure 2A). Further analysis
384 revealed that 72% of the HMW tau eluted consisted of AT8-positive species, while only 44% of the HMW
385 tau eluted were bioactive species. Intriguingly, while every fraction containing the bioactive species was
386 AT8 positive, we also observed non-bioactive AT8 positive species, accounting for 28% of the HMW tau
387 eluted. As expected, the bioactive AT8 positive species were eluted later compared to the AT8 negative
388 species. Importantly, we identified the same pattern of elution of non-bioactive and bioactive species for 9
389 AD cases with the exact same cut-off for the separation of the two species, with bioactive species eluting at
390 a NaCl concentration of 450 mM (Figure 2A, Supplemental Figure S3). This consistency among cases was
391 surprising considering the case-to-case variations in PTMs as noted in our prior mass spectroscopy analysis
392 using tissue from these same cases[23].

393 The linear gradient of elution separates the HMW tau population into multiple fractions, but mainly two
394 species are isolated, the non-bioactive and bioactive species. Therefore, considering the clear cut-off
395 between the non-bioactive and bioactive species, we performed a stepwise elution to separate both species
396 and collected each species within one fraction of 0.5 mL of buffer. In this strategy, both species are retained
397 on the AIEX column in Tris 20 mM pH8.6 as previously described, but for the elution, non-bioactive species
398 are eluted with a constant salt concentration of 0.3 M of NaCl and bioactive species are then eluted with 4M
399 of NaCl. Both fractions were then desalted into PBS. First, we evaluated the tau quantity in the fractions

400 corresponding to the two steps of elution by dot blot in native condition and we observed a similar tau
401 amount eluted in each step (Figure 2B). We then validated the separation of non-bioactive vs bioactive tau
402 species with a seeding assay showing a low bioactivity in the first step of elution comparatively to the high
403 seeding activity in the second step of elution, independently of the tau concentration (Figure 2B). We next
404 asked if the anion exchange chromatography separates two forms of tau or "peels" loosely bound tau from
405 an aggregated form of tau. To test this hypothesis, we injected both species into a SEC column to evaluate
406 the size and the associated seeding activity. Strikingly, the bioactive species contain only HMW tau species,
407 while the non-bioactive species contain a mixture of low and high molecular weight tau (Supplemental
408 Figure S4). Overall, these results suggest that the HMW tau population contains multiple subspecies
409 including non-bioactive and bioactive species that both co-elute from SEC in the HMW fractions but differ
410 by their retention time on an anion exchange column. We hypothesize that this behavior is due to a difference
411 in the number of charges, or a variety of conformations, or both.

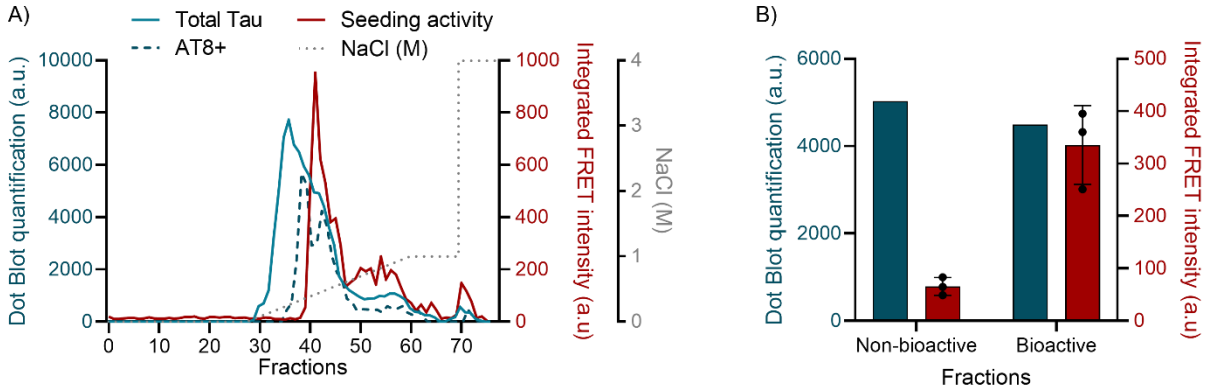

412

413 ***Figure 2. HMW tau fractionation by charge reveals seeding competent and inert species.***
414 *A) HMW tau fractionation originating from the AD case 1971 via anion exchange chromatography (AIEX)*
415 *with increasing NaCl concentration (gray dashed line). Tau and phosphorylated tau are measured in each*
416 *fraction by dot blot quantification using the pan-Tau antibody D5D8N (blue line) and AT8 antibody (dashed*
417 *blue line). Seeding activity of each fraction is determined using the FRET reporter HEK cell assay in*
418 *triplicate and measured by flow cytometry (red line). Data from one seeding assay, out of three, is plotted*
419 *as representative of the bioactivity profile. B) Separation of non-bioactive and bioactive HMW tau species,*
420 *originating from the AD case 1971 as in panel A, with AIEX via a step wise elution of NaCl. First-step*
421 *elution is performed with 0.3M NaCl followed by a second step of 4M NaCl. Non-bioactive and Bioactive*
422 *fractions are desalted into PBS before tau quantification on dot blot by the pan-Tau antibody D5D8N (blue)*
423 *and seeding activity assay measured by flow cytometry (red). Seeding assay data represent mean ± S.D. of*

424 *three individual experiments performed in triplicate, using non-bioactive and bioactive species isolated*
425 *from AD case 1971.*

426 **Both bioactive and non-bioactive HMW tau species consist of small diffusible aggregates**

427 We showed that the non-bioactive and bioactive species maintain their aggregate conformation after AIEX
428 and are consistently found in every AD case tested, hence we used one representative AD case (1971) to
429 carry the following biophysical and biochemical experiments. Given the ongoing debate in the field
430 regarding whether tau bioactive species are insoluble fibrils or small diffusible aggregates[26,27], we carried
431 out atomic force microscopy (AFM) of the samples deposited on freshly-cleaved mica surfaces
432 (representative AFM micrographs are shown in Figure 3A). The images clearly show the absence of fibrillar
433 structures, with mostly globular shapes, although these qualitatively differ for the bioactive and non-
434 bioactive samples. Particle size analysis of the AFM images of the bioactive and non-bioactive fractions
435 allowed us to extract two critical parameters, namely the equivalent radius (r_{eq}) and the maximum particle
436 height (Z_{max}), the distributions of which are shown in Figure 3B. Interestingly, we find a mono-exponential
437 distribution of r_{eq} values for both samples, with a decay constant of 2.65 nm and 3.72 nm for bioactive and
438 non-bioactive, respectively. However, analysis of Z_{max} values reveals two populations for each of the
439 samples, with a consistent cutoff maximum height of ~5 nm for both populations. Fitting the distributions
440 to bi-exponential functions, we find that the fraction of higher Z particles, F_2, is greater for the bioactive
441 particles (23±*1.16*%) than for the non-bioactive particles (2±*0.01%*), as calculated using $F_2 =$
442 $a_2z_2/(a_1z_1+a_2z_2)$, where a are the amplitudes and z are the decay constants obtained from the bi-exponential
443 fits. In summary, AFM did not show any fibrillar structures for either bioactive or non-bioactive particles,
444 and the observed particle size ranges are smaller than the sizes typically reported for fibrillar tau
445 aggregates[28,29]. To note, using human brain lysate from a control case, we observed similar size particles
446 with r_{eq} values ranging from 3 to 40 nm (Supplemental Figure S4).

447 To further characterize these samples, we performed transmission electron microscopy (TEM) combined
448 with tau-specific immunogold labeling. In both samples, immunogold confirmed the presence of tau clusters
449 with no detectable fibrils (Figure 3C). Interestingly, the distance between gold particles reveals different
450 patterns between the two species with higher number of dimers and linear trimers in the bioactive fraction,
451 Au-Au distance of 22.5 and 45.0 nm, respectively, than in the non-bioactive tau samples (Figure 3D). Of
452 note, we confirmed that the observed gold particles were due to tau presence rather than non-specific binding
453 of secondary antibodies by omitting the primary anti-tau antibody, which resulted in a low number of gold
454 particles. Moreover, analysis of the distances between gold particles revealed discrete values indicative of
455 dimers, trimers, and tetramers in the bioactive species, which were not detected in the non-bioactive species
456 (Figure 3). Tau observed across the micrographs did not display a uniform pattern, as would be expected

457 for monomeric soluble tau derived from a recombinant source or human brain control lysate (Supplemental
458 figure S6).

459 We also employed a recently developed single-molecule pull-down assay, which combines antibody-based
460 immunoprecipitation with single-molecule super-resolution fluorescence microscopy, to analyze tau
461 aggregates[18]. In this assay, tau aggregates are captured on an antibody-coated slide and detected using the
462 same monoclonal antibody fluorescently labeled. In this assay, an eccentricity above 0.9 indicates the
463 presence of fibrils[18]. Using this approach, we evaluated the eccentricity of both non-bioactive and bioactive
464 species with super-resolution microscopy, probing with HT7 and AT8 antibodies. In both cases, eccentricity
465 values were consistently below 0.9, indicating the presence of small amorphous aggregates.

466 Finally, upon fractionation of the non-bioactive and bioactive species by ultra-centrifugation 30 min at
467 100,000g at 4°C, we found that both species were present in the supernatant (Supplemental Figure S6).
468 Notably, the bioactivity of the bioactive species was retained in the supernatant. This result is consistent
469 with the presence of small diffusible aggregates and PBS soluble species. Overall, across three independent
470 methods, we consistently found that both species are composed of morphologically similar, but
471 biochemically distinct, small diffusible aggregates. While the negative stained EM images do not reveal
472 fibrils, we cannot rule out the presence of rare, short fibrils, and refer to these structures therefore as small
473 aggregates. Further studies including Cryo-EM would be necessary to obtain new insights and better
474 characterized the nature of these aggregates.

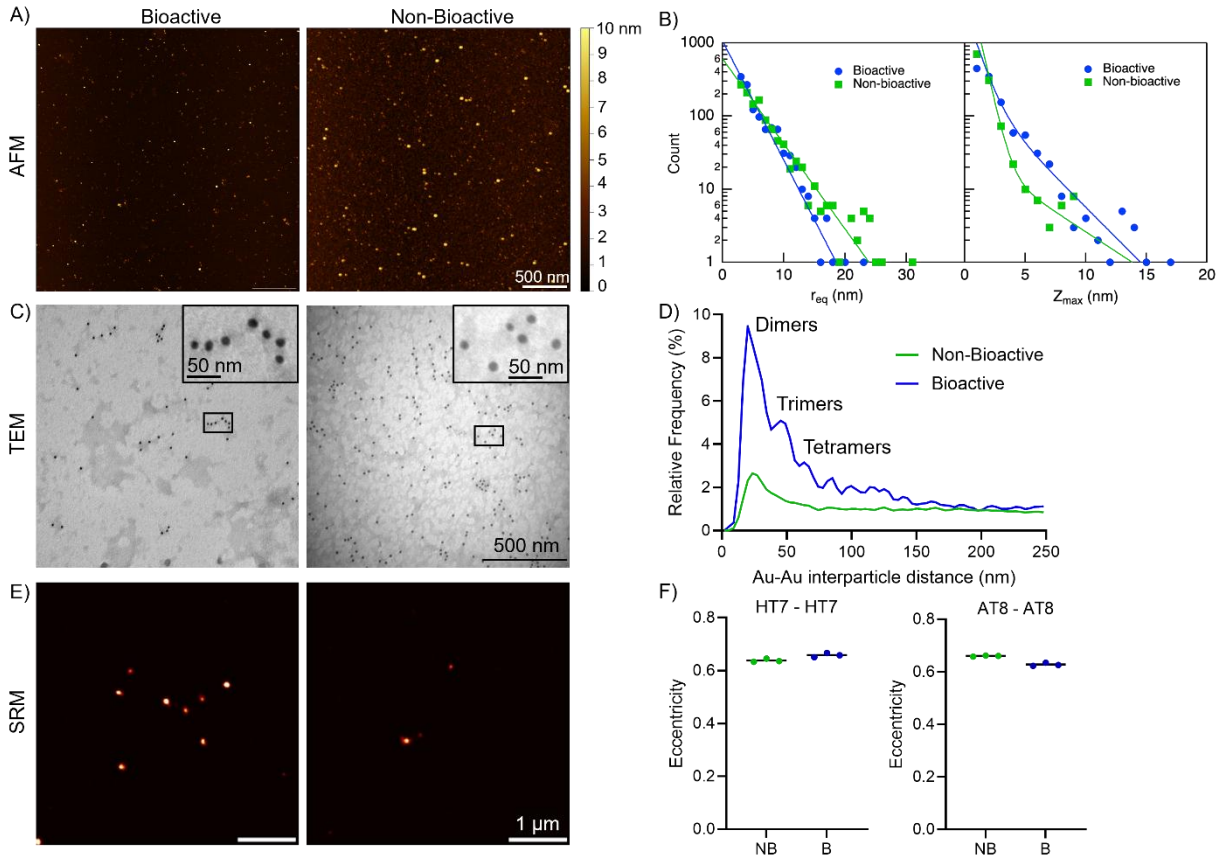

Figure 3. Non-bioactive and bioactive species contain small diffusible aggregates

A) Representative atomic force microscopy (AFM) images of bioactive and non-bioactive species isolated from the AD case 1971. B) AFM-based equivalent radius (r_{eq}) and maximum height (Z_{max}) distributions for non-bioactive (n = 1,141) and bioactive particles (n = 1,141), fit to single exponential and double exponential decaying functions, respectively. C) Representative transmission electron microscopy (TEM) immunogold images of bioactive and non-bioactive species labelled with the antibody pan-tau D5D8N and anti-rabbit secondary antibody conjugated with 12nm gold particles. Insets, representative gold particles pattern of non-bioactive and bioactive species. D) Analysis of the gold-gold distances from the center of particles. E) Representative super-resolution microscopy (SRM) images of bioactive and non-bioactive species captured and probed with AT8 antibody. F) Eccentricity quantification of HT7-HT7 and AT8-AT8 particles. Data represents mean of three individual measurements, conducted on non-bioactive and bioactive species isolated from the AD case 1971.

Non-bioactive and bioactive species differ in molecular conformations and phosphorylation status

We next further explored whether the bioactive and non-bioactive subfractions of the material eluting in the early fractions from size exclusion chromatography differ biochemically. We showed that these two species

491 can be separated by anion exchange chromatography, suggesting differences in net charge or the exposure
492 of charged regions. To explore these differences, we employed an ultrasensitive protein aggregate
493 quantification assay based on single molecule array (SIMOA) technology[19]. This assay captures and detects
494 tau aggregates using the same monoclonal antibody. Using the pan-tau antibody HT7, whose epitope is
495 similar as D5D8N, we evaluated the Tau aggregate content and we found that both species contained
496 aggregates, with higher levels in the bioactive species than in the non-bioactive species, 52.4 ng/mL and
497 27.4 ng/mL, respectively (Figure 4A). Interestingly, when we tested the MC1 antibody, developed to
498 recognize a unique conformation of tau present in PHF as well as earlier stages[30], it detected lower amounts
499 of aggregated tau (~5 ng/mL) than using the double monoclonal strategy in both species (Figure 4B). When
500 we assessed phosphorylated aggregates using AT8, p181, and p217 antibodies, the bioactive species showed
501 higher capture and detection signals. This indicates more exposed phosphorylation sites, which may explain
502 the increased retention time on the AIEX column. Finally, we evaluated the phosphorylation profile of
503 bioactive and non-bioactive Tau species from two AD cases using a combination of phospho-specific Tau
504 antibodies in dot blot analyses (Figure 4B). For quantification, the phospho-Tau signal was normalized to
505 the Tau signal detected by the pan-tau D5D8N antibody. Given that absolute signal intensities varied across
506 experiments while the relative signal between the non-bioactive and bioactive species remained consistent,
507 we compared, for each phosphosite, the phosphorylation signal ratio between the two species after
508 normalization to the bioactive species. Raw signals and inter-experiment variability are shown in
509 supplemental figures 7 and 8. Consistent with the SIMOA results, the dot blot quantification revealed that
510 bioactive species are more phosphorylated than their non-bioactive counterparts (Figure 4C, D). Notably,
511 for the AD case 1971 three antibodies targeting five phospho-sites pS202-pT205 (AT8), pT231, and pS396-
512 pS404 (PHF1) showed higher immunoreactivity in the bioactive species. This increase in phosphorylation
513 was even more pronounced for the bioactive species from AD case 2014, which displayed higher
514 immunoreactivity than the non-bioactive species at all AD case 1971 phosphosites as well as for pT181 and
515 pT231. These phosphorylation sites, located outside the AD fibril core region (amino acids 306–378), may
516 contribute to the retention of these species on the anion exchange column. Using the same dot-blot
517 quantification, we next estimated the relative phosphorylation burden of bioactive versus non-bioactive tau
518 more globally. Across all phospho-epitopes examined, non-bioactive species ranged from 0.04 to 0.9 when
519 expressed relative to the bioactive fraction (set to 1), corresponding to approximately 1- to 23-fold higher
520 phospho-signals in the bioactive species (Supplementary Table 1). When phospho-epitopes were considered
521 jointly, including the double-phospho antibodies AT8 and PHF1 but excluding the single-site pS396 and
522 pS404 antibodies that interrogate the same region, the composite phospho-signal was increased by ~4.5-
523 fold in the bioactive fraction for AD case 1971 and by ~7.8-fold for AD case 2014. Conversely, when we
524 considered pS396 and pS404 but excluded PHF1, the composite fold-change was 4.3 for AD case 1971 and

9.4 for AD case 2014. The similar values for AD case 1971 are consistent with both pS396 and pS404 showing comparably lower signals in the non-bioactive fraction, whereas the larger fold-change for AD case 2014 in this analysis is mainly driven by pS404. In AD case 1971, pS396-only and pS404-only antibodies each show modest, non-significant individual changes, but tau molecules phosphorylated at both sites (PHF1 epitope), as well as at AT8 and pT217, are clearly enriched in the bioactive fraction. In AD case 2014, tau molecules carrying pS404 alone and/or double phosphorylation at S396/S404 are enriched in the bioactive fraction in addition to those recognized by pT181, AT8, pT217 and pT231. Together, these data indicate that, although both species are phosphorylated and one is globally more phosphorylated than the other, clusters of phospho-modifications—rather than a uniform increase at individual sites—are preferentially enriched in the bioactive fraction. This is consistent with the non-bioactive and bioactive tau species differing in their surface available charge, phosphorylation status, and the likelihood of containing (at least) homodimers of phosphorylated tau.

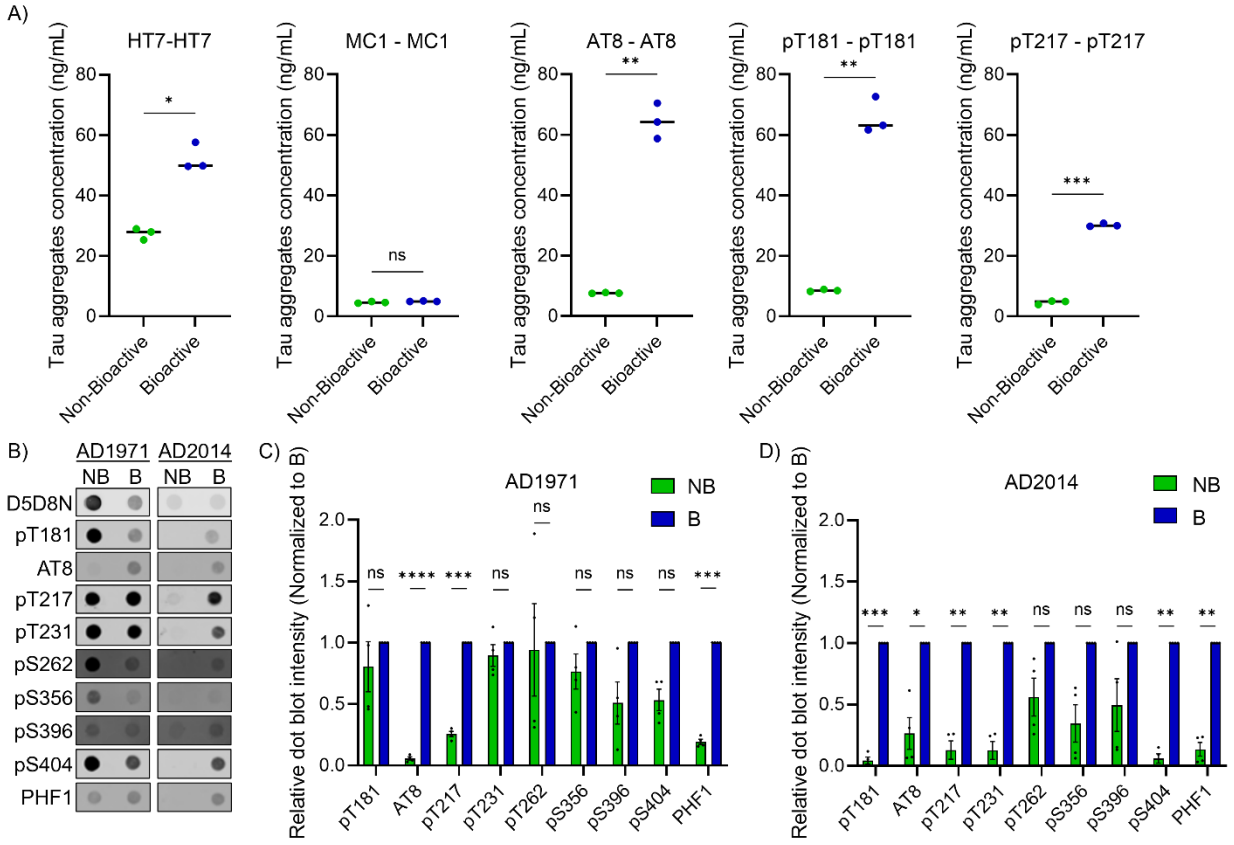

Figure 4. Tau Bioactive species exposes more phosphorylation sites.

*A) Tau aggregates concentration quantified by SIMOA assay using total tau antibody HT7, MC1, phospho-antibodies AT8, pT181 and pT217. Results were analyzed using the paired student t-test, * for $p < 0.05$, ** for $p < 0.01$, *** for $p < 0.001$, **** for $p < 0.0001$ and ns for non-significant. Experiments were conducted with non-bioactive and bioactive species extracted from AD case 1971. B) Dot blots of non-bioactive and bioactive species originating from two AD cases, probed with pan-Tau antibody D5D8Nalong with several anti-phospho Tau antibodies. C, D) Dot blots quantification, the anti-phospho Tau signal was adjusted to the signal obtain from the D5D8N pan-Tau antibody. Relative intensities of non-bioactive and bioactive species were determined from four independent experiments and normalized to the bioactive species (raw densitometry values are shown in figures S7 and S8). Non-bioactive and bioactive species are originating from two AD cases as indicated in panel B, C and D.*

Bioactive oligomeric tau is exceedingly potent

Based on the SIMOA experiment, we determined that the concentration of non-bioactive and bioactive species at 27.4 and 52.4 ng/mL, respectively, corresponding to approximately 12 ng of bioactive tau species per gram of frontal grey matter from a Braak VI case (i.e. pM concentrations). It is important to note, that these calculations were based on Tau species extracted from frontal cortex of Braak VI AD cases and hence Tau amounts might vary across brain regions and Braak stages. Given this low concentration, we investigated whether that low concentration could trigger aggregation in cells. Using the apparent molecular weight of HMW tau from SEC (~500 kDa), we calculated concentrations of 55 pM and 105 pM for the non-bioactive and bioactive species, respectively. These samples were then used to treat FRET reporter cells at decreasing concentrations. It is important to note that the tau species were diluted 19-fold with media and lipofectamine, resulting in maximum concentrations of 2900 fM and 5600 fM for the non-bioactive and bioactive species, respectively. Starting from these initial concentrations, we performed a 7-point twofold dilution series, with seeding detected at concentrations as low as 175 fM. For this analysis, we focused solely on the FRET signal intensity, disregarding the number of FRET-positive cells, to determine the minimum tau seed concentration required to induce aggregation. The cell-based assay isolates misfolded templating from cell uptake or escape from endosomal and lysosomal pathways, providing an estimate of the amount of seed competent tau which is the lower limit for a positive signal.

The data of the number of seeded cells as a function of tau oligomer concentration, are fit well by a "one hit model", i.e. a model in which a single seed is sufficient to induce daughter seeds in the reporter cells, consistent with predictions for prion-like behavior of the bioactive seeds (Fig 5B). We find that the seeding efficiency is more than 20-fold higher for the bioactive than the non-bioactive species, assuming the one hit model in both cases. This suggests that the bioactive seeds are at least an order of magnitude more potent than the non-bioactive seeds. It is important to note, however, that these calculations apply to a reporter

573 system engineered to efficiently amplify seeds, with excess truncated tau reporter present in the cytoplasm,
574 and access to the cytoplasm ensured by lipophilic reagents; in biological systems, the efficiency of seeding
575 would be expected to be substantially less.

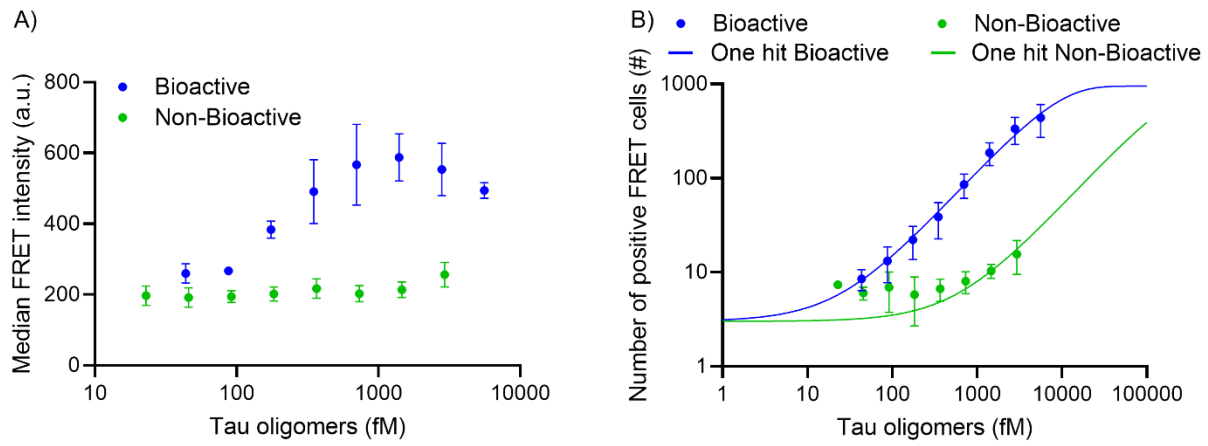

576

577 ***Figure 5. Seeding competency of bioactive tau.***
578 *A) Data represents the median ± S.D. FRET intensity and B) number ± S.D. of seeded cells measured from*
579 *three individual experiments performed in triplicate using the reporter HEK cell FRET assay with serially*
580 *diluted samples. The initial concentrations were 2900 fM for the non-bioactive species (green) and 5600 fM*
581 *for the bioactive species (blue), with each subsequent point representing a 1:2 dilution. Solid lines are fits*
582 *to a "one hit" model as detailed in the Methods. Experiments were conducted with non-bioactive and*
583 *bioactive species extracted from AD case 1971.*

584 **Brain derived bioactive oligomeric tau species support RT-QuIC amplification of truncated tau and**
585 **retain bioactivity in cellulo after amplification, unlike non-bioactive oligomers.**

586 In addition to assessing the high potency of the bioactive species in a cell reporter system, we also analyzed
587 their ability to generate fibrils in an isolated biochemical assay. To this end, we performed Real-Time
588 Quaking-Induced Conversion (RT-QuIC) assays to amplify and generate "daughter" bioactive seeds. We
589 then tested whether these newly formed seeds retained their bioactivity through a second round of
590 amplification via RT-QuIC. For the amplification, the AD core fragment (residues 306–378), which has
591 been previously validated in RT-QuIC assays to produce a ThT-positive signal, reflecting fibril formation,
592 when incubated with biological samples[20], was used as a substrate (Figure 6A). Interestingly, only the
593 bioactive species produced a detectable ThT signal consistent with the bioactive competency of these
594 species observed *in cellulo* (Figure 6B). By TEM we confirmed the presence of fibrillar structures (Figure
595 6D). After 72 hours, ThT-free reaction mixtures were collected and subjected to a second amplification with

596 fresh substrate. Similar to the first amplification, a ThT signal was observed only when daughter seeds were
597 formed with bioactive species, although with a longer lag phase (11.4 hours vs. 15.8 hours; Figure 6B, C).

598 Finally, we assessed the bioactivity of the daughter seeds generated after the first round of amplification *in*
599 *cellulo*. Daughter seeds derived from the bioactive species retained bioactivity, whereas material generated
600 from non-bioactive oligomers remained inactive, indicating that seeding-associated properties are preserved
601 over amplification (Figure 6E). Interestingly, when bioactive species were incubated with a mixture of
602 0N3R and 0N4R tau isoforms, we did not observe an increased ThT signal, but we did detect small
603 aggregates by TEM (Supplementary Figure S9). Moreover, the low seeding activity observed for the
604 daughter seeds generated using the 0N isoform mixture may be attributed to the absence of phosphorylation
605 sites on the recombinant substrates, as the 0N isoforms, expressed in *E. coli*, are not post-translationally
606 modified. Consequently, despite being aggregated by the bioactive species, these unmodified substrates may
607 lack the structural or biochemical features required to support efficient seeding. As expected, control lysate
608 did not generate a ThT signal with any of the substrates; this was also true for AD core or biological samples
609 alone, including those containing bioactive species (Supplemental Figure S10). Collectively, these results
610 show that brain-derived bioactive tau oligomers can template the aggregation of a naïve tau fragment in
611 vitro and propagate seeding activity across serial RT-QuIC amplification, with corresponding bioactivity in
612 a cellular assay—consistent with a prion-like, templated misfolding mechanism.

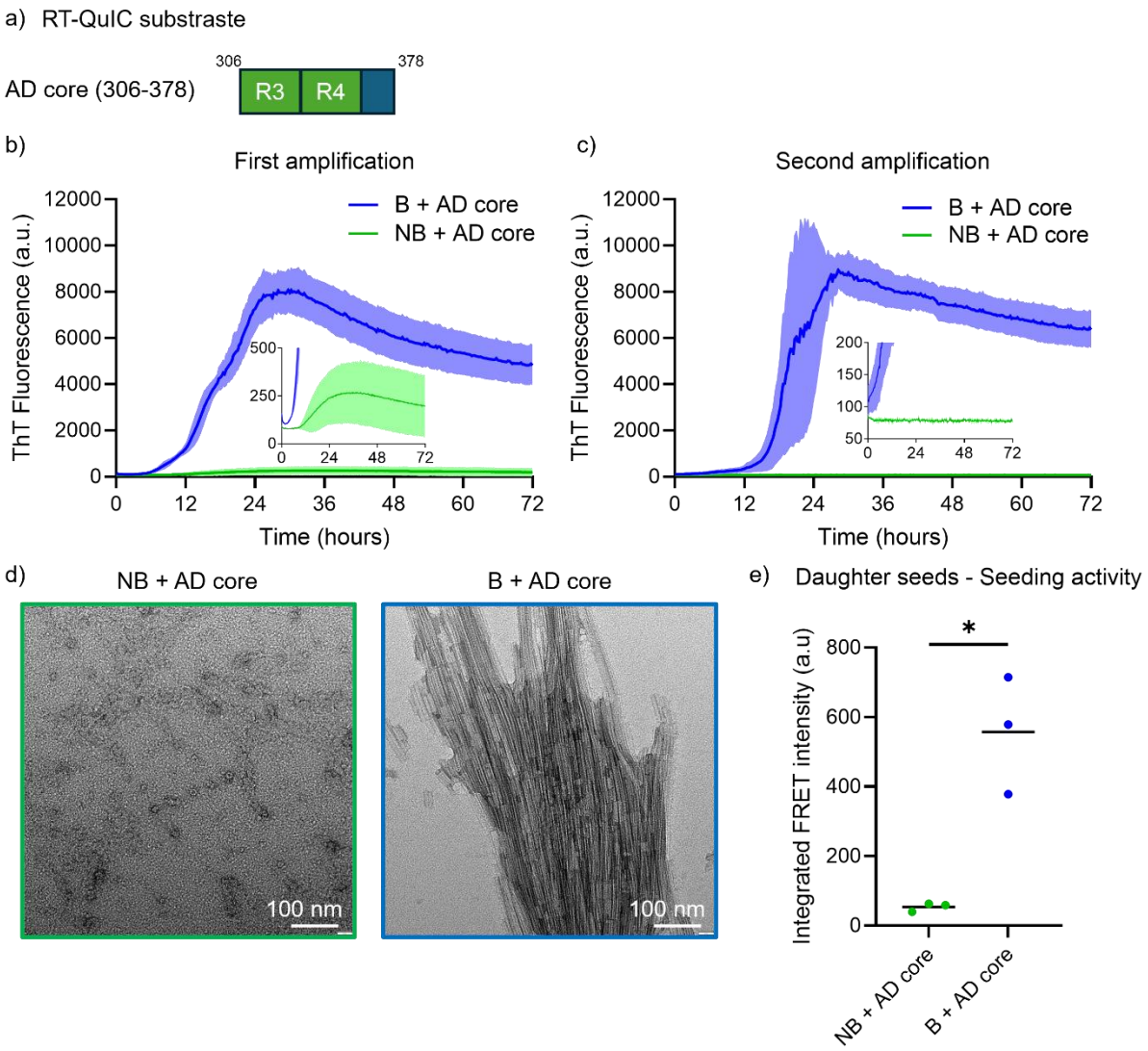

Figure 6. Bioactive species induce tau aggregation to generate seed competent daughters

A) Schematic representation of the AD core (residues 306-378) used as a substrate for RT-QuIC assays. A substrate concentration of 10 µM. B) RT-QuIC assays were performed by mixing AD core with non-bioactive (NB) and bioactive (B) species as seeds. C) RT-QuIC assays were performed with species formed after the 72 hours of incubation with both species and AD core acting as daughter seeds and fresh AD core. B, C) Data represents the mean ± S.D. of three individual experiments performed in triplicate. D) Representative negative-stain TEM images of daughter seeds formed with non-bioactive (NB) and bioactive (B) species after the first amplification (72h). E) Seeding activity of the daughter seeds (first amplification, 72h) is determined using the FRET reporter HEK cell assay and measured by flow cytometry. Data from three individual experiments are represented as mean, and analyzed using the paired student t-

624 *test, * for p < 0.05. Experiments were conducted on non-bioactive and bioactive species isolated from the*
625 *AD case 1971.*

626 **Discussion**

627 This study aimed to isolate, enrich, and identify bioactive diffusible tau aggregates implicated in AD
628 progression, providing insights into the biochemical features critical for tau seeding competency. Using 2D
629 gels and *in vitro* dephosphorylation, we confirmed that HMW tau comprises multiple subspecies, with
630 surface phosphorylated species identified as the bioactive subset, consistent with prior findings[16,22].

631 Anion exchange chromatography of human derived material revealed the presence of a myriad of HMW tau
632 species differing in charge and/or conformation. Given the extensive phosphorylation sites identified in
633 soluble tau across multiple AD cases—more than 20[23,30,31]—it is unsurprising that various combinations
634 might exist and yield multiple species. Nonetheless, this approach reproducibly separated non-bioactive and
635 bioactive HMW tau species across nine AD cases. This finding aligns with studies showing that aggregates
636 of the same protein can differ in biochemical properties and toxicity[32], that monomeric tau may adopt inert
637 and bioactive conformations in vitro[33], and that tau aggregates derived from different tauopathies vary in
638 conformation and bioactivity[34]. However, to our knowledge, this is the first demonstration that tau oligomers
639 isolated from individual human AD brains can differ so drastically in biochemical properties and seeding
640 competency.

641 The anion exchange chromatography data further suggests that the tau oligomers retained on the anion
642 exchange column are the most likely to seed aggregates. This implies that specific intracellular environments
643 or interactions may be critical for seeding. For instance, tau species with a pI above 7.4 would be positively
644 charged in the neuronal cytoplasm, while those with a pI below 7.4 would carry an atypical negative charge
645 for tau. We postulate that such heavily modified, negatively charged tau could recruit positively charged
646 tau, triggering aggregation. This is reinforced by the data shown in Fig 4, illustrating that the bioactive
647 fraction has phosphorylation epitopes detectable by dot blots and SIMOA assays that detect multimers that
648 are multiply phosphorylated. Indeed, using available anti-Tau phosphoepitopes we showed that bioactive
649 species were phosphorylated at positions T181, S202, T205, T217, T231, S262, S356, S396 and S404 with
650 stronger immunoreactivity for phosphosites T217, T231 and S404 comparatively to the non-bioactive
651 species, which could suggest that these epitopes are available for interaction with the anion exchange
652 column. While we cannot yet assign specific phospho-epitopes or define a phosphorylation signature for
653 seeding activity, our data indicate that phosphorylation clusters are enriched in the bioactive fraction and
654 seeding competence requires tau that is both assembled and highly phosphorylated. TEM and AFM are
655 label-free high-resolution methods, which rely on the drying of the sample on grids or mica. The affinity to

656 small and large aggregates varies, which causes higher or lower average values of the diameter of sampled
657 species compared to the distribution of the populations in solution. Conversely, single-molecule
658 fluorescence is insensitive to single monomers and capable of measuring the size of very large aggregates
659 at a scale of 200 × 200 µm skewing the average to larger values. Thus, although the exact measurements are
660 somewhat technique dependent, all three techniques used converge on the finding that the non-bioactive and
661 bioactive species are similar but not identical small aggregates that are nonfibrillar.

662 Combining these observations refines the characteristics that define seeding-competent tau. In our
663 preparations, both fractions consist of small, non-fibrillar oligomers, yet only the highly phosphorylated
664 bioactive oligomers are strongly seed-competent, whereas non-bioactive oligomers of comparable size show
665 little or no seeding activity. This supports the view that size or fibrillar status per se is not the primary
666 determinant of bioactivity and that phosphorylation acts as a key gating factor. This interpretation is
667 consistent with work on recombinant hyperphosphorylated tau, where multi-site phosphorylation is
668 sufficient to drive spontaneous aggregation into small, predominantly non-fibrillar oligomers that are more
669 toxic and more efficient at nucleating unmodified tau than unphosphorylated tau [35]. Recent single-molecule
670 AFM studies further show that hyperphosphorylation stabilizes smaller, stiffer and more adhesive tau
671 oligomers, supporting a model in which phosphorylation reshapes both the structural and mechanical
672 landscape of early aggregates in ways that favour pathogenic seeding[36]. Finally, studies using AD-derived
673 tau filaments have demonstrated that the fibril core structure alone is insufficient to recapitulate the seeding
674 potency of brain-derived material and that phosphorylation within the disordered fuzzy coat is required for
675 full seeding competency in neurons and *in vivo*[37]. Together, these findings and our own data converge on
676 the idea that tau seeding competence is best understood as a property of a restricted subset of aggregated
677 species that are both assembled and decorated with clustered phospho-epitopes, rather than a generic feature
678 of all oligomers or fibrils.

679 Our findings also demonstrate that tau recruitment and aggregation can occur at extremely low
680 concentrations of tau oligomers in the cytoplasm, where they encounter naïve tau. However, this bypasses
681 processes such as tau uptake and endolysosomal escape, which might necessitate higher concentrations, as
682 previously suggested[38]. Moreover, we showed that the small diffusible aggregated bioactive species induce
683 the formation of bioactive daughter seeds conversely to sarkosyl extracted fibrillar tau[39]. The low
684 concentration of seeds may explain the difficulties in developing a RT-QuIC assay for tau seeds in biofluids.

685 In previous studies we demonstrated by mass spectrometry that both the HMW fraction, (as well as an MC1
686 (conformationally specific tau antibody) immunoprecipitation fraction), contain a subset of the post
687 translational modifications that are present on sarkosyl insoluble fibrillar tau in AD[23,30], suggesting that the
688 HMW fraction is a form fruste of the fibrillar fraction. On the other hand, injection of HMW tau into h-tau

689 transgenic mice that express full length 3R and 4R tau[40], showed that the HMW fraction propagated across
690 neural systems but did not mature into sarkosyl insoluble fibrils over the course of 3 months. Our current
691 results suggest a possible way to resolve this discrepancy: in this study, truncated tau, rather than a mix of
692 3R/4R recombinant full length tau, supports fibril formation in the RT-QuIC assay, suggesting that the
693 conformation of the templated misfolding product is at least in part consequent to the specific substrate;
694 these results are broadly compatible with the cryo-EM studies of Lovestäm *et al.*, 2022[41], which
695 demonstrated that extending the amino acid sequence of recombinant tau beyond the core 297-391 fragment
696 impaired or dramatically altered fibril formation. These results also bring to mind the surprisingly sudden
697 appearance of tau fibrils in vivo (as observed by in vivo multiphoton microscopy) after protease activation
698 and appearance of cleaved tau[42], perhaps explaining the surprising and puzzling observation that the
699 extremely stable β pleated sheet containing tau fibrils can appear so quickly.

700 In the prion field, a "seed" is defined as a misfolded conformer of the prion protein capable of inducing the
701 misfolding of native prion molecules, with daughter seeds retaining the ability to propagate aggregation and
702 spread throughout the brain[43]. Owing to the parallels between prion propagation and tau aggregation, it has
703 been hypothesized that tau may spread via a prion-like mechanism[3]. Supporting this notion, it has been
704 demonstrated that tau seeds formed *in cellulo* can replicate and retain seeding competency over multiple
705 passages[44,45]. However, contrasting results have shown that Sarkosyl-insoluble extracts from Alzheimer's
706 disease (AD) brains can induce tau aggregation *in vitro*, yet the resulting daughter seeds may lack sustained
707 seeding competency[39]. These findings suggest that the mechanisms underlying tau seeding remain
708 incompletely understood—particularly regarding the precise identity of the tau species that initiate and
709 sustain this process. In this context, our fractionation and orthogonal imaging analyses indicate that seed
710 competence is not explained by an oligomeric form alone: both bioactive and non-bioactive HMW tau are
711 predominantly small assemblies (dimers–tetramers), yet only the bioactive subset retains robust activity in
712 vitro and in cellulo. This points to a two-component requirement for bioactivity, whereby tau must be
713 assembled into an aggregated state and must also carry specific biochemical attributes—most notably
714 features enriched in the anion-exchange–retained fraction and correlated with surface-accessible
715 phosphorylation—that distinguish seed-competent from seed-incompetent oligomers. Moreover, our
716 current data suggest that HMW bioactive seeds can induce seeding in reporter cells linearly related to
717 concentration (Fig 5B), consistent with a prion like behavior. It is important to note that the reporter cells
718 have been designed to maximize seeding efficiency, using lipofectamine to bypass uptake mechanisms and
719 an optimized truncated construct of the repeat domains to maximize aggregation. Thus, the current data
720 supports the biochemical idea of templated misfolding at very low concentrations, but do not speak to the
721 dose relevant for biological activity in an organism.

722 From a therapeutic perspective, effective tau-targeted therapies remain lacking[46]. In this study, we
723 established a protocol to extract small diffusible aggregates, stable forms of tau capable of inducing
724 aggregation, providing a foundation for developing reagents specifically targeting bioactive tau seeds in
725 AD.

726 Acknowledgement:

727 We acknowledge the use of the AFM instrument from the laboratory of Mark C. Williams at Northeastern
728 University and Dr. Mike Morse from Williams Lab for assistance with the AFM.

729 Funding:

730 This study was supported by the JPB Foundation, Massachusetts Alzheimer's Disease Research Center
731 (P30AG062421), RFI AG 079946 (LM), The Toffler Foundation, Cure Alzheimer's Fund, the Rainwater
732 Foundation and by the UK Dementia Research Institute through UK DRI Ltd, principally funded by the
733 Medical Research Council. DK holds a Royal Society funded Professorship. M. B. M. S. M. was supported
734 by the Elite Network of Bavaria (Elite Graduate Program Biomedical Neuroscience, S-LW-2016-351/2/58).

735 Authors contributions:

736 NQ, BTH, and DK conceived the study and designed the experiments. NQ, DS, DB, YC, JEC, AW, VD,
737 MBMSM, and FAB performed experiments and analyzed data. GM, MC and DGA developed mathematical
738 models for seeding and TEM analyses. TC, AM, MF and DO selected and provided human brain tissues.
739 The manuscript was written by NQ and BTH with input from all the authors.
740

741 Declaration of interests:

742 Dr. Hyman owns stock in Novartis; he serves on the SAB of Dewpoint and has an option for stock. He
743 serves on a scientific advisory board or is a consultant for AbbVie, Alexion, Ambagon, Aprinoia
744 Therapeutics, Arvinas, Avrobio, AstraZenica, Biogen, Bioinsights, BMS, Cell Signaling, Cure Alz Fund,
745 CurieBio, Dewpoint, Etiome, Latus, Merck, Novartis, Paragon, Pfizer, Sanofi, Sofinnova, SV Health,
746 Takeda, TD Cowen, Vigil, Violet, Voyager, WaveBreak. His laboratory is supported by research grants
747 from the National Institutes of Health, Cure Alzheimer's Fund, Tau Consortium, and the JPB Foundation –
748 and sponsored research agreement from Abbvie and Sanofi. Dr. Hyman and Dr. Frosch are part of a
749 Sponsored Research Agreement between Massachusetts General Hospital and Biogen as well as
750 Neurimmune. Dr. Oakley's immediate family owns stock in Biogen.
751
752
753

754 **References**

755 1. Arriagada, P.V., Marzloff, K., and Hyman, B.T. (1992). Distribution of Alzheimer-type
756 pathologic changes in nondemented elderly individuals matches the pattern in Alzheimer's
757 disease. Neurology *42*, 1681-1688. 10.1212/wnl.42.9.1681.
758 2. Gómez-Isla, T., Hollister, R., West, H., Mui, S., Growdon, J.H., Petersen, R.C., Parisi, J.E., and
759 Hyman, B.T. (1997). Neuronal loss correlates with but exceeds neurofibrillary tangles in
760 Alzheimer's disease. Annals of Neurology *41*, 17-24. https://doi.org/10.1002/ana.410410106.
761 3. Walker, L.C., Diamond, M.I., Duff, K.E., and Hyman, B.T. (2013). Mechanisms of protein
762 seeding in neurodegenerative diseases. JAMA Neurol *70*, 304-310.
763 10.1001/jamaneurol.2013.1453.
764 4. Iqbal, K., Liu, F., Gong, C.X., and Grundke-Iqbal, I. (2010). Tau in Alzheimer disease and related
765 tauopathies. Curr Alzheimer Res *7*, 656-664. 10.2174/156720510793611592.
766 5. Gerson, J.E., Castillo-Carranza, D.L., and Kayed, R. (2014). Advances in Therapeutics for
767 Neurodegenerative Tauopathies: Moving toward the Specific Targeting of the Most Toxic Tau
768 Species. ACS Chemical Neuroscience *5*, 752-769. 10.1021/cn500143n.
769 6. Shafiei, S.S., Guerrero-Muñoz, M.J., and Castillo-Carranza, D.L. (2017). Tau Oligomers:
770 Cytotoxicity, Propagation, and Mitochondrial Damage. Front Aging Neurosci *9*, 83.
771 10.3389/fnagi.2017.00083.
772 7. Berger, Z., Roder, H., Hanna, A., Carlson, A., Rangachari, V., Yue, M., Wszolek, Z., Ashe, K.,
773 Knight, J., Dickson, D., et al. (2007). Accumulation of pathological tau species and memory loss
774 in a conditional model of tauopathy. J Neurosci *27*, 3650-3662. 10.1523/jneurosci.0587-07.2007.
775 8. Lasagna-Reeves, C.A., Castillo-Carranza, D.L., Sengupta, U., Clos, A.L., Jackson, G.R., and
776 Kayed, R. (2011). Tau oligomers impair memory and induce synaptic and mitochondrial
777 dysfunction in wild-type mice. Mol Neurodegener *6*, 39. 10.1186/1750-1326-6-39.
778 9. Jiang, L., Ash, P.E.A., Maziuk, B.F., Ballance, H.I., Boudeau, S., Abdullatif, A.A., Orlando, M.,
779 Petrucelli, L., Ikezu, T., and Wolozin, B. (2019). TIA1 regulates the generation and response to
780 toxic tau oligomers. Acta Neuropathol *137*, 259-277. 10.1007/s00401-018-1937-5.
781 10. Zwang, T.J., Sastre, E.D., Wolf, N., Ruiz-Uribe, N., Woost, B., Hoglund, Z., Fan, Z., Bailey, J.,
782 Nfor, L., Buée, L., et al. (2024). Neurofibrillary tangle-bearing neurons have reduced risk of cell
783 death in mice with Alzheimer's pathology. Cell Rep *43*, 114574. 10.1016/j.celrep.2024.114574.
784 11. Hyman, B.T., Van Hoesen, G.W., Wolozin, B.L., Davies, P., Kromer, L.J., and Damasio, A.R.
785 (1988). Alz-50 antibody recognizes Alzheimer-related neuronal changes. Ann Neurol *23*, 371-
786 379. 10.1002/ana.410230410.
787 12. Maeda, S., Sahara, N., Saito, Y., Murayama, S., Ikai, A., and Takashima, A. (2006). Increased
788 levels of granular tau oligomers: an early sign of brain aging and Alzheimer's disease. Neurosci
789 Res *54*, 197-201. 10.1016/j.neures.2005.11.009.
790 13. DeVos, S.L., Corjuc, B.T., Oakley, D.H., Nobuhara, C.K., Bannon, R.N., Chase, A., Commins,
791 C., Gonzalez, J.A., Dooley, P.M., Frosch, M.P., and Hyman, B.T. (2018). Synaptic Tau Seeding
792 Precedes Tau Pathology in Human Alzheimer's Disease Brain. Front Neurosci *12*, 267.
793 10.3389/fnins.2018.00267.
794 14. Dujardin, S., Commins, C., Lathuiliere, A., Beerepoot, P., Fernandes, A.R., Kamath, T.V., De Los
795 Santos, M.B., Klickstein, N., Corjuc, D.L., Corjuc, B.T., et al. (2020). Tau molecular diversity
796 contributes to clinical heterogeneity in Alzheimer's disease. Nat Med *26*, 1256-1263.
797 10.1038/s41591-020-0938-9.
798 15. Sepulveda-Falla, D., Chavez-Gutierrez, L., Portelius, E., Vélez, J.I., Dujardin, S., Barrera-
799 Ocampo, A., Dinkel, F., Hagel, C., Puig, B., Mastronardi, C., et al. (2021). A multifactorial model
800 of pathology for age of onset heterogeneity in familial Alzheimer's disease. Acta Neuropathol *141*,
801 217-233. 10.1007/s00401-020-02249-0.
802 16. Takeda, S., Wegmann, S., Cho, H., DeVos, S.L., Commins, C., Roe, A.D., Nicholls, S.B.,
803 Carlson, G.A., Pitstick, R., Nobuhara, C.K., et al. (2015). Neuronal uptake and propagation of a

rare phosphorylated high-molecular-weight tau derived from Alzheimer's disease brain. Nat Commun *6*, 8490. 10.1038/ncomms9490.

17. Braak, H., and Braak, E. (1991). Neuropathological stageing of Alzheimer-related changes. Acta Neuropathol *82*, 239-259. 10.1007/bf00308809.

18. Böken, D., Cox, D., Burke, M., Lam, J.Y.L., Katsinelos, T., Danial, J.S.H., Fertan, E., McEwan, W.A., Rowe, J.B., and Klenerman, D. (2024). Single-Molecule Characterization and Super-Resolution Imaging of Alzheimer's Disease-Relevant Tau Aggregates in Human Samples. Angew Chem Int Ed Engl *63*, e202317756. 10.1002/anie.202317756.

19. Böken, D., Xia, Z., Lam, J.Y.L., Fertan, E., Wu, Y., English, E.A., Konc, J., Layburn, F., Bernardes, G.J.L., Zetterberg, H., et al. (2025). Ultrasensitive Protein Aggregate Quantification Assays for Neurodegenerative Diseases on the Simoa Platform. Anal Chem *97*, 290-299. 10.1021/acs.analchem.4c04188.

20. Carlomagno, Y., Manne, S., DeTure, M., Prudencio, M., Zhang, Y.J., Hanna Al-Shaikh, R., Dunmore, J.A., Daughrity, L.M., Song, Y., Castanedes-Casey, M., et al. (2021). The AD tau core spontaneously self-assembles and recruits full-length tau to filaments. Cell Rep *34*, 108843. 10.1016/j.celrep.2021.108843.

21. Holmes, B.B., Furman, J.L., Mahan, T.E., Yamasaki, T.R., Mirbaha, H., Eades, W.C., Belaygorod, L., Cairns, N.J., Holtzman, D.M., and Diamond, M.I. (2014). Proteopathic tau seeding predicts tauopathy in vivo. Proc Natl Acad Sci U S A *111*, E4376-E4385. 10.1073/pnas.1411649111.

22. Wu, R., Li, L., Shi, R., Zhou, Y., Jin, N., Gu, J., Tung, Y.C., Liu, F., and Chu, D. (2021). Dephosphorylation Passivates the Seeding Activity of Oligomeric Tau Derived From Alzheimer's Brain. Frontiers in Molecular Neuroscience *14*. 10.3389/fnmol.2021.631833.

23. Kumar, M., Quittot, N., Dujardin, S., Schlaffner, C.N., Viode, A., Wiedmer, A., Beerepoot, P., Chun, J.E., Glynn, C., Fernandes, A.R., et al. (2024). Alzheimer proteopathic tau seeds are biochemically a forme fruste of mature paired helical filaments. Brain *147*, 637-648. 10.1093/brain/awad378.

24. Vandebroek, T., Vanhelmont, T., Terwel, D., Borghgraef, P., Lemaire, K., Snauwaert, J., Wera, S., Van Leuven, F., and Winderickx, J. (2005). Identification and Isolation of a Hyperphosphorylated, Conformationally Changed Intermediate of Human Protein Tau Expressed in Yeast. Biochemistry *44*, 11466-11475. 10.1021/bi0506775.

25. Tepper, K., Biernat, J., Kumar, S., Wegmann, S., Timm, T., Hübschmann, S., Redecke, L., Mandelkow, E.M., Müller, D.J., and Mandelkow, E. (2014). Oligomer formation of tau protein hyperphosphorylated in cells. J Biol Chem *289*, 34389-34407. 10.1074/jbc.M114.611368.

26. Stern, A.M., and Selkoe, D.J. (2023). Soluble oligomers or insoluble fibrils? Scientific commentary on "Tau seeding and spreading in vivo is supported by both AD-derived fibrillar and oligomeric tau". Acta Neuropathol *146*, 861-862. 10.1007/s00401-023-02633-6.

27. Mate de Gerando, A., Quittot, N., Frosch, M.P., and Hyman, B.T. (2023). Reply: Soluble oligomers or insoluble fibrils? Acta Neuropathol *146*, 863-866. 10.1007/s00401-023-02634-5.

28. Wegmann, S., Muller, D.J., and Mandelkow, E. (2012). Investigating fibrillar aggregates of Tau protein by atomic force microscopy. Methods Mol Biol *849*, 169-183. 10.1007/978-1-61779-551-0_12.

29. Hussong, S.A., Banh, A.Q., Van Skike, C.E., Dorigatti, A.O., Hernandez, S.F., Hart, M.J., Ferran, B., Makhlouf, H., Gaczynska, M., Osmulski, P.A., et al. (2023). Soluble pathogenic tau enters brain vascular endothelial cells and drives cellular senescence and brain microvascular dysfunction in a mouse model of tauopathy. Nature Communications *14*, 2367. 10.1038/s41467-023-37840-y.

30. Wesseling, H., Mair, W., Kumar, M., Schlaffner, C.N., Tang, S., Beerepoot, P., Fatou, B., Guise, A.J., Cheng, L., Takeda, S., et al. (2020). Tau PTM Profiles Identify Patient Heterogeneity and Stages of Alzheimer's Disease. Cell *183*, 1699-1713 e1613. 10.1016/j.cell.2020.10.029.

31. Kyalu Ngoie Zola, N., Balty, C., Pyr dit Ruys, S., Vanparys, A.A.T., Huyghe, N.D.G., Herinckx, G., Johanns, M., Boyer, E., Kienlen-Campard, P., Rider, M.H., et al. (2023). Specific post-translational modifications of soluble tau protein distinguishes Alzheimer's disease and primary tauopathies. Nature Communications *14*, 3706. 10.1038/s41467-023-39328-1.
32. Limbocker, R., Cremades, N., Cascella, R., Tessier, P.M., Vendruscolo, M., and Chiti, F. (2023). Characterization of Pairs of Toxic and Nontoxic Misfolded Protein Oligomers Elucidates the Structural Determinants of Oligomer Toxicity in Protein Misfolding Diseases. Acc Chem Res *56*, 1395-1405. 10.1021/acs.accounts.3c00045.
33. Hitt, B.D., Gupta, A., Singh, R., Yang, T., Beaver, J.D., Shang, P., White, C.L., 3rd, Joachimiak, L.A., and Diamond, M.I. (2023). Anti-tau antibodies targeting a conformation-dependent epitope selectively bind seeds. J Biol Chem *299*, 105252. 10.1016/j.jbc.2023.105252.
34. Lo Cascio, F., Park, S., Sengupta, U., Puangmalai, N., Bhatt, N., Shchankin, N., Jerez, C., Moreno, N., Bittar, A., Xavier, R., et al. (2025). Brain-derived tau oligomer polymorphs: distinct aggregations, stability profiles, and biological activities. Commun Biol *8*, 53. 10.1038/s42003-025-07499-w.
35. Meng, J.X., Zhang, Y., Saman, D., Haider, A.M., De, S., Sang, J.C., Brown, K., Jiang, K., Humphrey, J., Julian, L., et al. (2022). Hyperphosphorylated tau self-assembles into amorphous aggregates eliciting TLR4-dependent responses. Nat Commun *13*, 2692. 10.1038/s41467-022-30461-x.
36. Pillai, V.V.S., Smeding, T., Meng, J.X., Klenerman, D., and Ruggeri, F.S. (2025). Single-Oligomer Characterization of Tau Phosphorylation and Mechanical State. ACS Meas Sci Au *5*, 951-962. 10.1021/acsmeasuresciau.5c00116.
37. Kasen, A., Lövestam, S., Breton, L., Meyerdirk, L., McPhail, J.A., Piche, K., Louwrier, A., Capan, C.D., Lee, H., Scheres, S.H.W., and Henderson, M.X. (2025). Seed structure and phosphorylation in the fuzzy coat impact tau seeding competency. Nat Commun *16*, 9240. 10.1038/s41467-025-64312-2.
38. Miller, L.V.C., Mukadam, A.S., Durrant, C.S., Vaysburd, M.J., Katsinelos, T., Tuck, B.J., Sanford, S., Sheppard, O., Knox, C., Cheng, S., et al. (2021). Tau assemblies do not behave like independently acting prion-like particles in mouse neural tissue. Acta Neuropathol Commun *9*, 41. 10.1186/s40478-021-01141-6.
39. Duan, P., Dregni, A.J., Xu, H., Changolkar, L., Lee, V.M.Y., Lee, E.B., and Hong, M. (2024). Alzheimer’s disease seeded tau forms paired helical filaments yet lacks seeding potential. Journal of Biological Chemistry *300*. 10.1016/j.jbc.2024.107730.
40. Mate de Gerando, A., Khasnavis, A., Welikovitch, L.A., Bhavsar, H., Glynn, C., Quittot, N., Perbet, R., and Hyman, B.T. (2024). Aqueous extractable nonfibrillar and sarkosyl extractable fibrillar Alzheimer's disease tau seeds have distinct properties. Acta Neuropathol Commun *12*, 145. 10.1186/s40478-024-01849-1.
41. Lövestam, S., Koh, F.A., van Knippenberg, B., Kotecha, A., Murzin, A.G., Goedert, M., and Scheres, S.H.W. (2022). Assembly of recombinant tau into filaments identical to those of Alzheimer's disease and chronic traumatic encephalopathy. eLife *11*, e76494. 10.7554/eLife.76494.
42. de Calignon, A., Fox, L.M., Pitstick, R., Carlson, G.A., Bacskai, B.J., Spires-Jones, T.L., and Hyman, B.T. (2010). Caspase activation precedes and leads to tangles. Nature *464*, 1201-1204. 10.1038/nature08890.
43. Zampar, S., Di Gregorio, S.E., Grimmer, G., Watts, J.C., and Ingelsson, M. (2024). "Prion-like" seeding and propagation of oligomeric protein assemblies in neurodegenerative disorders. Frontiers in Neuroscience *Volume 18 - 2024*. 10.3389/fnins.2024.1436262.
44. Sanders, D.W., Kaufman, S.K., DeVos, S.L., Sharma, A.M., Mirbaha, H., Li, A., Barker, S.J., Foley, A.C., Thorpe, J.R., Serpell, L.C., et al. (2014). Distinct tau prion strains propagate in cells and mice and define different tauopathies. Neuron *82*, 1271-1288. 10.1016/j.neuron.2014.04.047.

904 45. Huang, M., and McEwan, W.A. (2025). Sensitive detection and propagation of brain-derived tau
905 assemblies in HEK293-based wild-type tau seeding assays. Journal of Biological Chemistry *301*.
906 10.1016/j.jbc.2025.108245.
907 46. Congdon, E.E., Ji, C., Tetlow, A.M., Jiang, Y., and Sigurdsson, E.M. (2023). Tau-targeting
908 therapies for Alzheimer disease: current status and future directions. Nature Reviews Neurology
909 *19*, 715-736. 10.1038/s41582-023-00883-2.

910